

Spatial inhomogeneity and the metal-insulator transition in $\text{Ca}_3(\text{Ru}_{1-x}\text{Ti}_x)_2\text{O}_7$

Frank Lechermann,¹ Qiang Han,² and Andrew J. Millis^{2,3}

¹*I. Institut für Theoretische Physik, Universität Hamburg, Jungiusstrasse 9, 20355 Hamburg, Germany*

²*Department of Physics, Columbia University, 538 West 120th Street, New York, NY 10027, USA*

³*Center for Computational Quantum Physics, The Flatiron Institute, 162 5th Avenue, New York, NY 10010, USA*

(Dated: September 29, 2020)

Turning a pristine Mott insulator into a correlated metal by chemical doping is a common procedure in strongly correlated materials physics, e.g. underlying the phenomenology of high- T_c cuprates. The ruthenate bilayer compound $\text{Ca}_3\text{Ru}_2\text{O}_7$ is a prominent example of a reversed case, namely a correlated metal at stoichiometry that realizes a transition into an insulating state via Ti doping. We here investigate this puzzling metal-insulator transition (MIT) by first-principles many-body theory and elucidate a challenging interplay between electronic correlations and symmetry breakings on the Ru sublattice. While average effects on the $\text{Ca}_3\text{Ru}_2\text{O}_7$ crystal structure are still relevant, key to the MIT is the cooperation of electronic correlations with the spatial inhomogeneity in the defect regime. Together they give rise to the emergence of site-selective Mott criticality and competing orbital-ordering tendencies.

Introduction.— The interplay of various degrees of freedom, e.g. of charge, orbital, spin or structural kind, is key to an understanding of many realistic metal-insulator transitions (MITs) in nature¹. In this respect, the Ruddlesden-Popper series of n -layered calcium ruthenates $\text{Ca}_{n+1}\text{Ru}_n\text{O}_{3n+1}$ poses a particularly challenging problem. It is agreed that electronic correlations arise from low-spin $\text{Ru}^{4+}(4d^4)$ sites in these compounds, formally locating them in a Hund-metal²⁻⁴ regime. While the $n \rightarrow \infty$ perovskite CaRuO_3 is metallic⁵ with competing magnetic interactions⁶ down to lowest temperatures, distorted Ca_2RuO_4 ($n=1$) undergoes a paramagnetic MIT at $T_{\text{MIT}} = 357$ K and displays antiferromagnetic (AFM) order below $T_N = 110$ K⁷. From these limiting cases, Mott criticality is expectedly intricate in the bilayer system. And indeed, though $\text{Ca}_3\text{Ru}_2\text{O}_7$ shows several electronic and magnetic transitions for $T < 100$ K⁸⁻¹², a robust insulating state is not reached at stoichiometry. With its non-centrosymmetric $Bb2_1m$ space group, the bilayer ruthenate marks the case of a 'polar metal'¹³⁻¹⁵, and has gained recent strong interest due to a complex fermiology^{10,16-18}.

Doping of about 5% titanium gives rise to a MIT in the bilayer compound^{12,19} at $T_{\text{MIT}} \sim 80$ K. The magnetic order switches from the stoichiometric A-type ordering of AFM-coupled ferromagnetic bilayers to G-type AFM ordering. There is apparently no paramagnetic Mott-insulating phase in $\text{Ca}_3(\text{Ru}_{1-x}\text{Ti}_x)_2\text{O}_7$. Weakly-localized states are already observed for very small Ti doping²⁰, and perculative behavior is also detected¹². According to Ke *et al.*¹⁹, the substitutional dopants enter as $\text{Ti}^{4+}(3d^0)$ impurities, therefore do not provide any significant charge doping. Hence the doping-induced MIT has originally been associated with the blocking of hopping paths¹⁹. Furthermore, the averaged crystal structure of the Ti-doped bilayer¹² displays also an enhanced two-dimensionality of the bilayers as well as a somewhat increased tilting of the RuO_6 octahedra. These global structural changes lead to a larger averaged crystal-field (CF) splitting Δ between the three partially occupied $\text{Ru}(4d)$ states $m = xy, xz/yz$ of t_{2g} character. In fact, a large Δ is the major driving force for the MIT in Ca_2RuO_4 ^{21,22}.

Since the energy scales in $\text{Ca}_3\text{Ru}_2\text{O}_7$ are generally smaller than in the latter single-layer ruthenate, the competition between the various degrees of freedom is much more subtle.

In this work, the goal is to unveil the detailed cooperation of defect physics and electronic correlations that drive the MIT in Ti-doped $\text{Ca}_3\text{Ru}_2\text{O}_7$. By means of the real-space combination of density functional theory (DFT) and dynamical mean-field theory (DMFT) applied to a defect supercell with 6.25% Ti concentration in a fully charge self-consistent manner, we profoundly account for average and local effects on an equal footing. While average effects from doping are notable, the spatial inhomogeneity introduced by Ti defects and cooperating with electron correlations is the crucial driving force towards the insulating phase.

Theoretical approach.— Charge self-consistent DFT+DMFT²³⁻²⁵ is used to access the correlated electronic structure. For the DFT part, a mixed-basis pseudopotential method^{26,27}, employing the generalized-gradient approximation in the Perdew-Burke-Ernzerhof form²⁸, is put into practise. Spin-orbit coupling is neglected in this work. The multi-single-site DMFT impurity problems encountered in the basic unit cell as well as in the defect supercell are solved by the hybridization-expansion continuous-time quantum Monte Carlo scheme²⁹, as implemented in the TRIQS code^{30,31}. The correlated subspace consists of the effective transition-metal (TM) t_{2g} Wannier-like functions $w_m(t_{2g})$, i.e. covers locally three orbitals. These functions are obtained from the projected-local-orbital formalism^{32,33}, using as projection functions the linear combinations of atomic-like t_{2g} orbitals that diagonalize the TM local $w_m(t_{2g})$ -orbital density matrix on each site.

Local Coulomb interactions in general Slater-Kanamori form, i.e. including density-density as well as spin-flip and pair-hopping terms, are parametrized by a Hubbard U and a Hund's exchange J_H . The intraorbital interaction U on the Ru sites is treated as a parameter, ranging at most from 1.5 eV to 7.5 eV. The Hund's exchange is chosen $J_H = 0.4$ eV for $U < 2$ eV and $J_H = 0.7$ eV for $U > 2$ eV, in order to allow for comparison with previous theory work on ruthenates²¹. For the Ti sites, a value $U = 5$ eV (and $J_H = 0.7$ eV) is cho-

sen to account for the fact that interactions in the Ti(3d) shell may be larger than in the Ru(4d) shell. To obtain the spectral information, analytical continuation from Matsubara space by the maximum-entropy method and the Padé method is performed.

Stoichiometric $\text{Ca}_3\text{Ru}_2\text{O}_7$.— To set the stage, we start with the correlated electronic structure of stoichiometric $\text{Ca}_3\text{Ru}_2\text{O}_7$. Figure 1a displays the experimental unit cell¹³ at 40 K with inplane lattice parameters $a = 5.37 \text{ \AA}$, $b = 5.54 \text{ \AA}$ and $c = 19.52 \text{ \AA}$. It incorporates two bilayers along the c -axis and a total of 8 Ru sites. The relevant CF splitting Δ in the t_{2g} manifold of the Ru(4d) states is defined as $\Delta = \varepsilon_{xy} - (\varepsilon_{xz} + \varepsilon_{yz})/2$, where ε_m are the CF levels of the xy, xz, yz Wannier orbitals. Effects due to the small splitting between xz, yz states are minor and will not be discussed henceforth (though the corresponding splitting is surely included in the calculations). On the DFT level, the bare CF splitting amounts to $\Delta = -153 \text{ meV}$, i.e. the xy state is low-

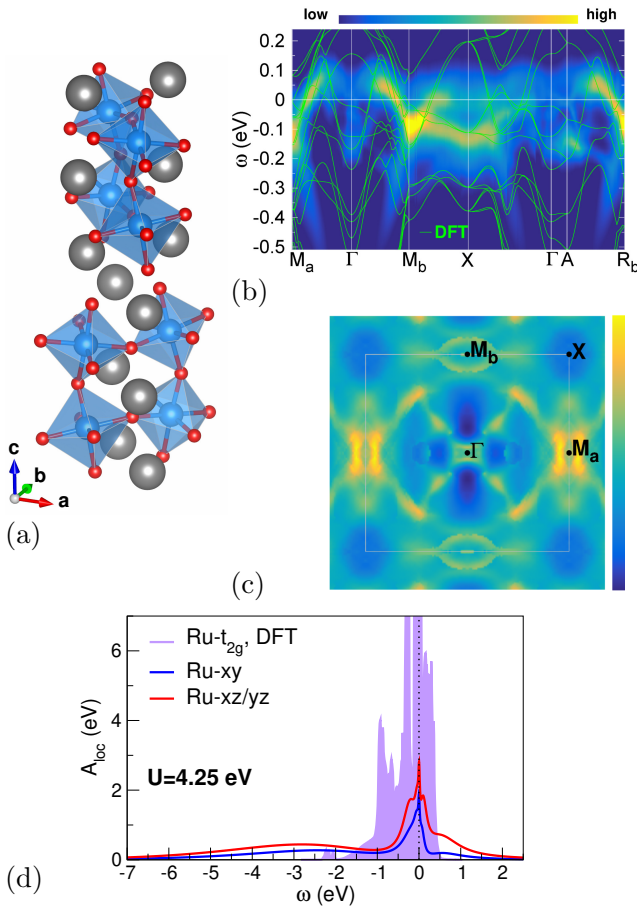


FIG. 1. (color online) Characterization of stoichiometric $\text{Ca}_3\text{Ru}_2\text{O}_7$. (a) Unit cell with two bilayers; Ca (large grey), Ru (blue) and O (small red). (b-d) Paramagnetic DFT+DMFT results for $U = 4.25 \text{ eV}$ at $T = 100 \text{ K}$. (b) Spectral function $A(\mathbf{k}, \omega)$ along high-symmetry lines, compared to DFT bands (green). (c) Fermi surface in $k_z = 0$ plane, gray rectangular marks the Brillouin zone. (d) Local Ru- t_{2g} spectral function discriminating the xy and xz/yz orbitals and comparing to DFT spectrum.

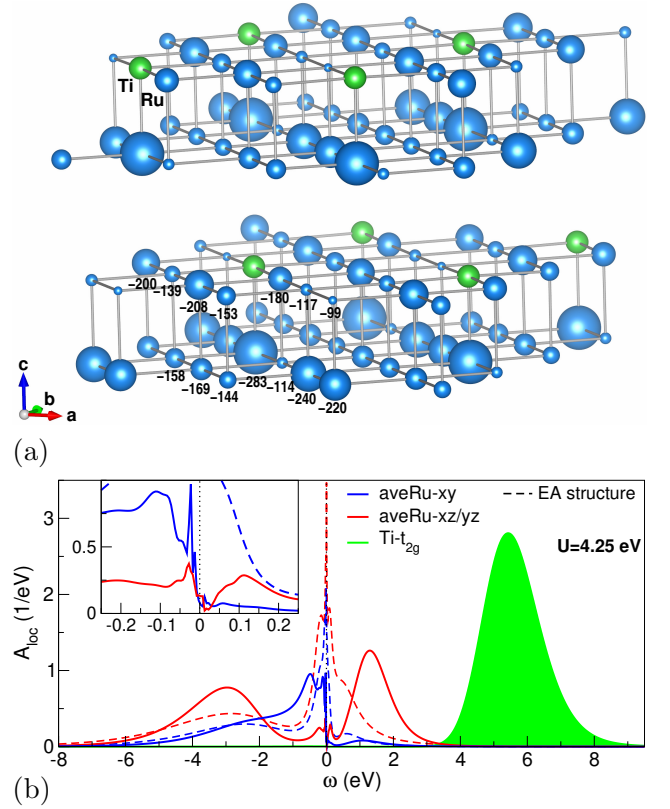


FIG. 2. (color online) Structure and global spectrum of $\text{Ca}_3(\text{Ru}_{0.9375}\text{Ti}_{0.0625})_2\text{O}_7$. (a) Structurally relaxed supercell showing Ru (blue) and Ti (green) ions, indicating the crystal-field splitting Δ via the diameter of the Ru-site spheres (Ca and O sites are not shown). Numbers indicate the actual Δ value of a given Ru-site symmetry class (in meV). The diameter of the Ti spheres is chosen as the average Δ of the Ru sites. (b) Average Ru(4d)- t_{2g} and Ti(3d)- t_{2g} paramagnetic local spectrum with 6.25% Ti for $U = 4.25 \text{ eV}$ ($T = 40 \text{ K}$). Dashed lines show the corresponding Ru- t_{2g} spectrum of the EA structure for comparison. Inset: blow up of the low-energy region.

est in energy. This results in an orbital polarization, giving rise to occupations $n_{xy} = 1.43$ and $n_{xz/yz} = 1.26$ per orbital. Note that the given CF splitting is about half the value of $\Delta \sim -320 \text{ meV}$ in single-layer Ca_2RuO_4 ²¹.

The correlated spectral data at $T = 100 \text{ K}$ is depicted in Figs. 1b-d. The compound is metallic, but compared to DFT, strong renormalization and loss of coherence is revealed at low energy, in accordance with angle-resolved photoemission^{10,16,17}. Significant inplane anisotropy in the correlated fermiology takes place between M_a and M_b , in line with experiment¹⁰. A more thorough investigation of further lower-temperature dispersions asks for an inclusion of spin-orbit coupling, and is not an objective of the present study. Finally, the local spectral functions show that the xz/yz states are stronger correlated with a lower Hubbard band of enhanced weight and deeper energy location of $\sim -2.9 \text{ eV}$ than the xy states.

Local electronic structure of $\text{Ca}_3(\text{Ru}_{0.9375}\text{Ti}_{0.0625})_2\text{O}_7$.— In

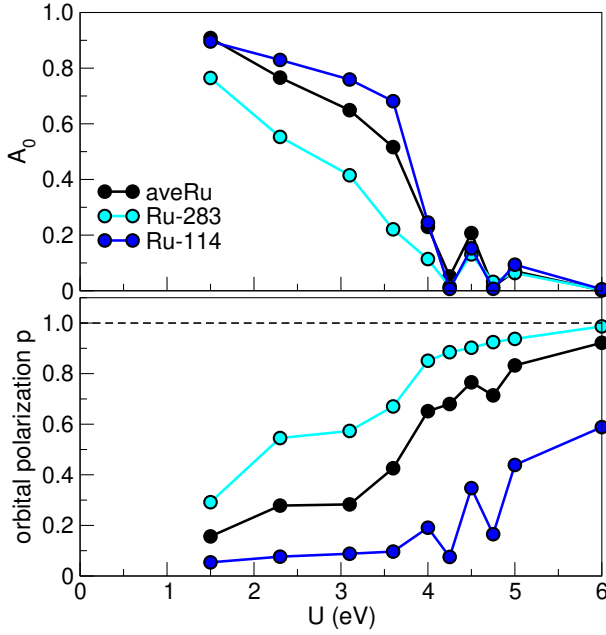


FIG. 3. (color online) The Ru(4d)- t_{2g} spectral weight A_0 at the Fermi level (top) and the orbital polarization p (bottom) with increasing U , for selected Ru-site classes in the Ti-doped supercell, respectively, at $T = 40$ K.

order to describe the bilayer ruthenate with finite Ti doping, we start from the experimentally-averaged (EA) structure at 10 K with 5% Ti doping¹⁹. The corresponding experimental system is insulating below $T_{MIT} \sim 80$ K. As an averaged structure, the atom-number size of the primitive cell is identical to the one at stoichiometry, but with different lattice parameters $a = 5.38$ Å, $b = 5.56$ Å and $c = 19.37$ Å, as well as modified atomic positions. Thus the effect of Ti impurities is only taken into account implicitly via an averaged structure modification. The effective CF splitting in this structure amounts to $\Delta = -171$ eV in DFT, hence is about 20 meV larger than in the stoichiometric case. This is mainly attributed to an enhanced two-dimensionality and increased tilting of the RuO_6 octahedra. It can be seen from the dashed lines in Fig. 2b that this treatment of Ti doping is not sufficient to render the system insulating for a reasonable value of $U = 4.25$ eV, but electronic correlations are somewhat enhanced compared to the stoichiometric case.

Let us turn to the supercell description of Ti-doped $\text{Ca}_3\text{Ru}_2\text{O}_7$. A 192-atom-site cell (cf. Fig. 2a) is constructed, starting from the EA structure and introducing two Ti impurities in adjacent bilayers, i.e. each bilayer carries one substitutional Ti defect. There are 32 TM sites in the defect supercell, 30 of Ru and 2 of Ti kind. Fixing the scaled EA lattice parameters, we structurally relax this supercell within DFT+U assuming G-type AFM order. No symmetry constraints are enforced in the structural relaxation. This leads to site-symmetry breakings, not unexpected in this puzzling polar-metal system³⁴. For the DFT+DMFT investigation at a system temperature of $T = 40$ K, we identify 14 Ru-site classes as symmetry inequivalent. Together with

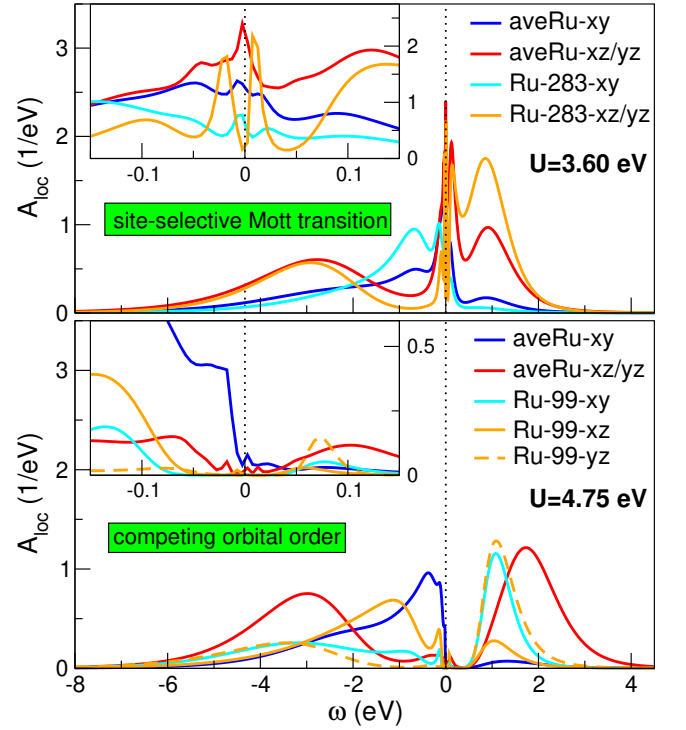


FIG. 4. (color online) Local Ru(4d)- t_{2g} spectral function for $U = 3.60$ eV (top) and $U = 4.75$ eV (bottom) at $T = 40$ K. The average spectra and two selected Ru-site class spectra are shown, respectively: For Ru-283(Ru-99) at the lower(larger) U value.

both symmetry-equivalent Ti sites, there are hence 15 coupled impurity problems solved at each self-consistency step.

As in previous DFT calculations¹⁹, the Ti impurities are indeed of $\text{Ti}^{4+}(3d^0)$ kind, and the t_{2g} electronic spectrum is accordingly located high in energy within the unoccupied region (see green part in Fig. 2b). Note that local structural relaxation shifts the Ti spectrum to somewhat smaller energies. The resulting CF splitting on the Ru sites is however distributed over a surprisingly large energy window $[-99, -283]$ eV. In order to simplify notation, we will in the following address the different Ru-site classes as 'RuΔ'. Interestingly, the Ru sites just below the Ti impurities have the largest CF splitting. These Ru-283 sites show a comparatively large relaxation *away* from Ti. The latter may be explained by the fact that due to the $3d^0$ character of titanium, the effective xz/yz hopping perpendicular to the plane is strongly weakened, resulting also in an overall reduced Ru-Ti bonding. Hence, the original effect of Ti sites blocking hopping paths is affirmed, however this single-particle-based mechanism alone cannot be sufficient to drive the MIT at the given comparatively small amounts of doping.

Notably, the average DFT crystal-field splitting in the supercell amounts to $\Delta_{av} = -172$ eV and is thus indeed identical to the one in the starting EA structure. But for equal local Coulomb interactions, the system is Mott insulating with strong orbital polarization as shown in Fig. 2b. On average, the xy state becomes fully occupied and the xz/yz states each host one electron, such that the four-electron oc-

cupation of $\text{Ru}(4d)-t_{2g}$ is realized. This orbital-polarization scenario is reminiscent of the one in single-layer Cu_2RuO_4 ²¹. But since the average CF splittings of the EA structure and the aligned supercell correspond to each other, the spatial inhomogeneity has to play a key role in the bilayer MIT.

The site-selective data shown in Fig. 3 and corresponding electronic spectra in Fig. 4 render indeed obvious, that the various Ru sites behave quite differently, in connection with their respective Δ value. In order to not only rely on analytical continuation, Ru local spectral weight at lowest energy, i.e. $A_{\text{loc}}(\omega)$ at zero frequency $\omega = 0$, is plotted in the top of Fig. 3 in its approximate form $A_0 = -\frac{\beta}{\pi} \sum_m \text{Im} G_{\text{loc}}^{(m)}(\beta/2)$, where $G_{\text{loc}}^{(m)}(\tau)$ is the local one-particle Green's function for orbital m and imaginary times τ at inverse temperature $\beta = 1/T$. The Ru-283 sites are much stronger correlated than e.g. the Ru-99 or Ru-114 sites with small Δ . In fact, for $U = 3.6$ eV the former sites have already gapped Ru- t_{2g} states, while on average, the Ru sublattice still shows metallic response (see inset in top of Fig. 4). The wide spectrum of CF values based on the significant spatial inhomogeneity introduced by Ti doping therefore gives rise to a site-selective Mott scenario^{35,36} in $\text{Ca}_3(\text{Ru}_{0.9375}\text{Ti}_{0.0625})_2\text{O}_7$. It occurs on the Ru sites perpendicular-adjacent to the Ti impurities and is precursory to the MIT of the complete system at $U \sim 4$ eV.

Nonsurprisingly, the orbital polarization, here simply defined as $p = n_{xy} - (n_{xz} + n_{yz})/2$, is much weaker for small- Δ sites. Those sites also cause site-selective physics, namely an oscillatory-in- U revival of metallicity for $U > 4$ eV. Only for $U = 6$ eV all sites behave insulating 'in line'. The given intermediate large U -regime can be traced back to strong orbital(-order) competition originating from the small- Δ Ru sites. On average close to the metal-insulator transition, the xy orbital becomes completely filled with two electrons, whereas the xz, yz become half filled, resulting in $p = 1$. However, e.g. the Ru-99 sites mark a dominant xz and close to half-filled yz, xy orbital filling for $U = 4.75$ eV (see bottom of Fig. 4).

In order to render the comparison between the spatial homogeneous and -inhomogeneous case more explicit, Fig. 5 displays the $-\Delta$ vs. U phase diagram of effective Ti-doped $\text{Ca}_3\text{Ru}_2\text{O}_7$. It is constructed by utilizing the EA structure and gradually fixing Δ within the DFT+DMFT calculations. Note that charge self-consistency is an important ingredient, since orbital polarization and MIT tendencies depend thereon³⁷. Since the true experimental system is AFM ordered in the insulating phase, results for G-AFM order of the EA structure are included. Those were obtained by enabling a spin-polarized self-energy in the DFT+DMFT cycle. As expected, the MIT occurs at somewhat smaller U with G-AFM order, yet the net effect of magnetic ordering on the Mott criticality is not decisive. Increasing the absolute value of Δ fosters the driving toward the MIT, but the slope remains steep for $-\Delta < 200$ meV. The MIT occurs for moderate U values only for rather large CF splittings. Note in this respect that a paramagnetic MIT was realized for single-layer Ca_2RuO_4 with $\Delta \sim -320$ meV for $U = 3.1$ eV in a previous one-shot DFT+DMFT calculation²¹. But such one-shot approaches are known for two features compared to charge

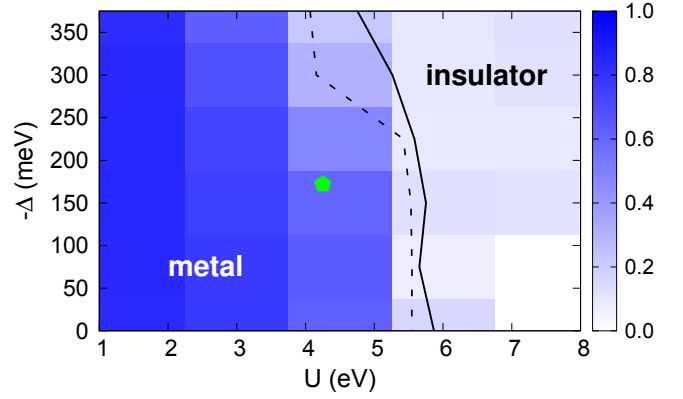


FIG. 5. Crystal-field vs. U phase diagram for Ti-doped $\text{Ca}_3\text{Ru}_2\text{O}_7$ based on the EA structure at $T = 100$ K (see text for further details). Blue color scale amounts to A_0 of $\text{Ru}(4d)-t_{2g}$ in the PM regime. Full(Dashed) line marks the interpolated metal-insulator phase boundary, here roughly defined by $A_0 = 0.2$, in the PM(G-AFM) regime. Green pentagon marks the position of the onset of the insulating phase in the supercell calculations (here located via its average Δ value).

self-consistent DFT+DMFT^{37,38}, namely tending to overestimate orbital polarizations and often realizing smaller critical U values. Furthermore, the MIT value of $U = 4.25$ eV for the defect supercell (see green pentagon in Fig. 5) is still well in the metallic region of the EA-based phase diagram. Yet remember that the 'orbital-competing regime' up to a robust spatially-coherent insulating state extends also up to $U = 6$ eV in the supercell calculations. Still, it may be inferred that spatial inhomogeneity, which is not included in the EA structure, is proactive in driving the MIT toward smaller U values.

We moreover performed DFT+DMFT calculations with allowing for AFM ordering in the Ti-doped supercell. Also there, competing orderings, now between different AFM tendencies occur: while or moderate $3 < U < 4$ eV the system tends to A-type like ordering, reminiscent of the stoichiometric magnetic order, for $U > 4$ eV indeed G-type like ordering becomes more favorable. Above $U = 6$ eV a very robust G-AFM ordering pattern is established.

Summary.— By means of large-scale first-principles many-body calculations, we showed that the MIT in Ti-doped $\text{Ca}_3\text{Ru}_2\text{O}_7$ is mainly driven by the interplay of spatial-inhomogeneity features and strong electronic correlations. Introduction of Ti impurities leads to a substantial energy spread of the CF splitting Δ across the Ru sublattice, resulting in site-selective Mott transitions for large- Δ sites and competitions in the orbital-ordering tendencies on small- Δ sites. This explains not only the occurrence of a doping-induced metal-insulator transition for reasonable interaction strengths, but accounts furthermore for the findings of percolative behavior. Other effects such as hopping-blocking or average structural modification via a change of lattice parameters furthermore support the insulating tendencies with doping, but appear not decisive. The here reported site-selective physics may also be relevant for an understand-

ing and modelling of recently discovered current-induced diamagnetism³⁹ in Ti-doped $\text{Ca}_3\text{Ru}_2\text{O}_7$. Describing the transport scenario from a possibly current-induced (partial-)gap closing and/or the coexistence of diamagnetism with persisting (local) magnetic order, could rely on the important interplay of electronic correlation and spatial inhomogeneity. Furthermore concerning experiments, scanning-tunneling studies of $\text{Ca}_3(\text{Ru}_{1-x}\text{Ti}_x)_2\text{O}_7$ would be highly interesting to verify the here unveiled site-dependent Mott physics.

Let us finally emphasize that sole averaged-structure investigations of defect problems in correlated materials may have their shortcomings. In a recent realistic DMFT study on impurities in V_2O_3 ³⁷, it was shown that local point-group symmetry breaking from trigonal to monoclinic is essential to understand the Cr-induced paramagnetic MIT. And here,

Ti-induced site-symmetry breakings are key to the MIT in $\text{Ca}_3\text{Ru}_2\text{O}_7$. Both results corroborate that the explicit and detailed cooperation of defect chemistry and many-body physics is at the heart of various doping problems in correlated matter.

ACKNOWLEDGMENTS

F.L. acknowledges financial support from the German Science Foundation (DFG) via the project LE-2446/4-1. A.J.M. acknowledges support from the Basic Energy Sciences program of the US Department of Energy under grant SC-0018218. Computations were performed at the University of Hamburg and the JUWELS Cluster of the Jülich Supercomputing Centre (JSC) under project number hhh08.

- ¹ Q. Han and A. Millis, Phys. Rev. Lett. **121**, 067601 (2018).
- ² P. Werner, E. Gull, M. Troyer, and A. J. Millis, Phys. Rev. Lett. **101**, 166405 (2008).
- ³ K. Haule and G. Kotliar, New J. Phys. **11**, 025021 (2009).
- ⁴ L. de Medici, J. Mravlje, and A. Georges, Phys. Rev. Lett. **107**, 256401 (2011).
- ⁵ Q. Han, H. T. Dang, and A. J. Millis, Phys. Rev. B **93**, 155103 (2016).
- ⁶ T. He and R. J. Cava, Phys. Rev. B **63**, 172403 (2001).
- ⁷ C. S. Alexander, G. Cao, V. Dobrosavljevic, S. McCall, J. E. Crow, E. Lochner, and R. P. Guertin, Phys. Rev. B **60**, R8422 (1999).
- ⁸ G. Cao, S. McCall, J. E. Crow, and R. P. Guertin, Phys. Rev. Lett. **78**, 1751 (1997).
- ⁹ Y. Yoshida, I. Nagai, S.-I. Ikeda, N. Shirakawa, M. Kosaka, and N. Môri, Phys. Rev. B **69**, 220411 (2004).
- ¹⁰ F. Baumberger, N. J. C. Ingle, N. Kikugawa, M. A. Hossain, W. Meevasana, R. S. Perry, K. M. Shen, D. H. Lu, A. Damascelli, A. Rost, A. P. Mackenzie, Z. Hussain, and Z.-X. Shen, Phys. Rev. Lett. **96**, 107601 (2006).
- ¹¹ J. S. Lee, S. J. Moon, B. J. Yang, J. Yu, U. Schade, Y. Yoshida, S.-I. Ikeda, and T. W. Noh, Phys. Rev. Lett. **98**, 097403 (2007).
- ¹² J. Peng, X. Ke, G. Wang, J. E. Ortmann, D. Fobes, T. Hong, W. Tian, X. Wu, and Z. Q. Mao, Phys. Rev. B **87**, 085125 (2013).
- ¹³ Y. Yoshida, S.-I. Ikeda, H. Matsuhata, N. Shirakawa, C. H. Lee, and S. Katano, Phys. Rev. B **72**, 054412 (2005).
- ¹⁴ D. J. Singh and S. Auluck, Phys. Rev. Lett. **96**, 097203 (2006).
- ¹⁵ F. Thöle and N. A. Spaldin, Phil. Trans. R. Soc. A **376**, 20170450 (2018).
- ¹⁶ M. Horio, Q. Wang, V. Granata, K. P. Kramer, Y. Sassa, S. Jöhr, D. Sutter, A. Bold, L. Das, Y. Xu, R. Frison, R. Fittipaldi, T. K. Kim, C. Cacho, J. E. Rault, P. L. Fèvre, F. Bertran, N. C. Plumb, M. Shi, A. Vecchione, M. H. Fischer, and J. Chang, arXiv:1911.12163 (2019).
- ¹⁷ I. Marković, M. D. Watson, O. J. Clark, F. Mazzola, E. A. Morales, C. A. Hooley, H. Rosner, C. M. Polley, T. Balasubramanian, S. Mukherjee, N. Kikugawa, D. A. Sokolov, A. P. Mackenzie, and P. D. C. King, arXiv:2001.09499 (2020).
- ¹⁸ D. Puggioni, M. Horio, J. Chang, and J. M. Rondinelli, Phys. Rev. Research **2**, 023141 (2020).
- ¹⁹ X. Ke, J. Peng, D. J. Singh, T. Hong, W. Tian, C. R. Dela Cruz, and Z. Q. Mao, Phys. Rev. B **84**, 201102 (2011).
- ²⁰ S. Tsuda, N. Kikugawa, K. Sugii, S. Uji, S. Ueda, M. Nishio, and Y. Maeno, Phys. Rev. B **87**, 241107 (2013).
- ²¹ E. Gorelov, M. Karolak, T. O. Wehling, F. Lechermann, A. I. Lichtenstein, and E. Pavarini, Phys. Rev. Lett. **104**, 226401 (2010).
- ²² A. Liebsch and H. Ishida, Phys. Rev. Lett. **98**, 216403 (2007).
- ²³ S. Y. Savrasov, G. Kotliar, and E. Abrahams, Nature **410**, 793 (2001).
- ²⁴ L. V. Pourovskii, B. Amadon, S. Biermann, and A. Georges, Phys. Rev. B **76**, 235101 (2007).
- ²⁵ D. Grieger, C. Piefke, O. E. Peil, and F. Lechermann, Phys. Rev. B **86**, 155121 (2012).
- ²⁶ F. Lechermann, F. Welsch, C. Elsässer, C. Ederer, M. Fähnle, J. M. Sanchez, and B. Meyer, Phys. Rev. B **65**, 132104 (2002).
- ²⁷ B. Meyer, C. Elsässer, F. Lechermann, and M. Fähnle, *FORTRAN 90 Program for Mixed-Basis-Pseudopotential Calculations for Crystals*, Max-Planck-Institut für Metallforschung, Stuttgart (1998).
- ²⁸ J. P. Perdew, K. Burke, and M. Ernzerhof, Phys. Rev. Lett. **77**, 3865 (1996).
- ²⁹ P. Werner, A. Comanac, L. de' Medici, M. Troyer, and A. J. Millis, Phys. Rev. Lett. **97**, 076405 (2006).
- ³⁰ O. Parcollet, M. Ferrero, T. Ayrat, H. Hafermann, I. Krivenko, L. Messio, and P. Seth, Comput. Phys. Commun. **196**, 398 (2015).
- ³¹ P. Seth, I. Krivenko, M. Ferrero, and O. Parcollet, Comput. Phys. Commun. **200**, 274 (2016).
- ³² B. Amadon, F. Lechermann, A. Georges, F. Jollet, T. O. Wehling, and A. I. Lichtenstein, Phys. Rev. B **77**, 205112 (2008).
- ³³ V. I. Anisimov, D. E. Kondakov, A. V. Kozhevnikov, I. A. Nekrasov, Z. V. Pchelkina, J. W. Allen, S.-K. Mo, H.-D. Kim, P. Metcalf, S. Suga, A. Sekiyama, G. Keller, I. Leonov, X. Ren, and D. Vollhardt, Phys. Rev. B **71**, 125119 (2005).
- ³⁴ A. Gangshettiwar, Y. Zhu, Z. Jiang, J. Peng, Y. Wang, J. He, J. Zhou, Z. Mao, and K. Lai, arXiv:2002.10489 (2020).
- ³⁵ H. Park, A. J. Millis, and C. A. Marianetti, Phys. Rev. Lett. **109**, 156402 (2012).

- ³⁶ F. Lechermann and M. Obermeyer, *New Journal of Physics* **17**, 043026 (2015).
- ³⁷ F. Lechermann, N. Bernstein, I. I. Mazin, and R. Valentí, *Phys. Rev. Lett.* **121**, 106401 (2018).
- ³⁸ A. Hampel, S. Beck, and C. Ederer, *Phys. Rev. Research* **2**, 033088 (2020).
- ³⁹ C. Sow, R. Numasaki, G. Mattoni, S. Yonezawa, N. Kikugawa, S. Uji, and Y. Maeno, *Phys. Rev. Lett.* **122**, 196602 (2019).